Proceedings of SPIE, Vol. 4742, April 2002

Technical Issues Associated with the Detection of Buried Land Mines with High-Frequency Seismic Waves

Seung-Ho Lee[a], Waymond R. Scott, Jr.[a],
James S. Martin[b], Gregg D. Larson[b], and George S. McCall II[c]

[a]School of Electrical and Computer Engineering
[b]School of Mechanical Engineering
[c]Georgia Tech Research Institute
Georgia Institute of Technology
Atlanta, GA 30332-0250

ABSTRACT

An array of radars is developed as a stand off sensor for use in elastic/seismic mine detection systems. The array consists of N radar sensors which operate independently to sense the displacement of the surface of the earth due to elastic waves propagating in the earth. Each of the sensors consists of a lens-focused, conical, corrugated, horn antenna and a homodyne radar. The focused antenna allows the sensor to have greater standoff than with the previous unfocused antenna while maintaining the spatial resolution required for a mine detection system. By using an array of N sensors instead of a single sensor, the scan rate of the array is improved by a factor of N. A theoretical model for the focused antenna is developed and an array of two radars is developed and used to validate the theoretical model. This array is tested in both the experimental and the field models for the elastic mine detection system. Results from both systems are presented.

Keywords: Mine Detection, Seismic Waves, Elastic Waves, Radar, Array.

1. INTRODUCTION

Recent research has shown that elastic/seismic detection techniques show great promise for the detection of buried land mines. However, significant technical problems must be overcome to make a practical mine detection system that uses these waves. The technical problems include 1) the measurement of elastic waves with sufficient accuracy and spatial resolution to detect small mines while achieving a measurement speed consistent with operational requirements, 2) the generation of soil-borne elastic waves in a robust and repeatable manner over all types of terrain, and 3) the integration of sources, sensors, and signal processing in a way that will result in the most effective system. The development of an appropriate sensor to sense the seismic waves is one of the biggest technical challenges. Various sensors can and have been used: laser doppler vibometers,[1,2] radar,[3,4] ultrasonic sensors,[5] air-acoustic displacement sensors,[6,7] ground contacting probes such as accelerometers,[8] etc. Of the non-contact sensors only the radar has been shown to be able to function effectively with a significant layer of vegetation on the surface of the ground.[9] In this paper, the development of an array of radar sensors to measure the elastic waves in the ground is described.

In earlier papers, the results from a single radar sensor that used an open ended waveguide as an antenna have been presented. This radar system performed well, but had two significant issues for a practical mine detection system: The antenna for this radar had to be placed within a few centimeters from the surface to get the required spatial resolution and the scanning speed was very slow. Both of these issues are addressed in this paper. A focused antenna is developed which increases the standoff distance from a couple centimeters to 20 cm while maintaining sufficient spatial resolution. Preliminary results for this antenna were presented last year[9]; in this paper, the theoretical model, design, and performance of the antenna have been improved. To improve the scanning speed, an array of N independent radar sensors is developed, allowing the displacements of the surface to be measured at N positions simultaneously which results in a factor of N increase in scanning speed.

A schematic diagram of a two element array incorporated in a elastic/seismic system is shown in Fig. 1. Here an elastic wave transducer is placed on the ground and induces an elastic wave into the earth. The wave causes both

E-mail and Tel.: W. R. Scott, Jr.: waymond.scott@ece.gatech.edu, 404-894-3048

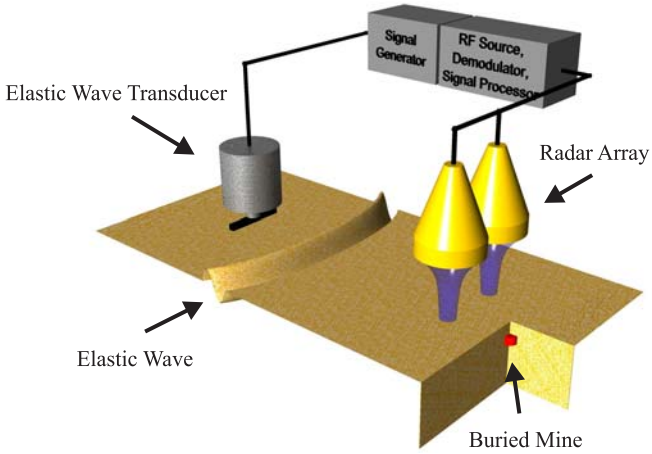

Figure 1. A diagram of the radar array.

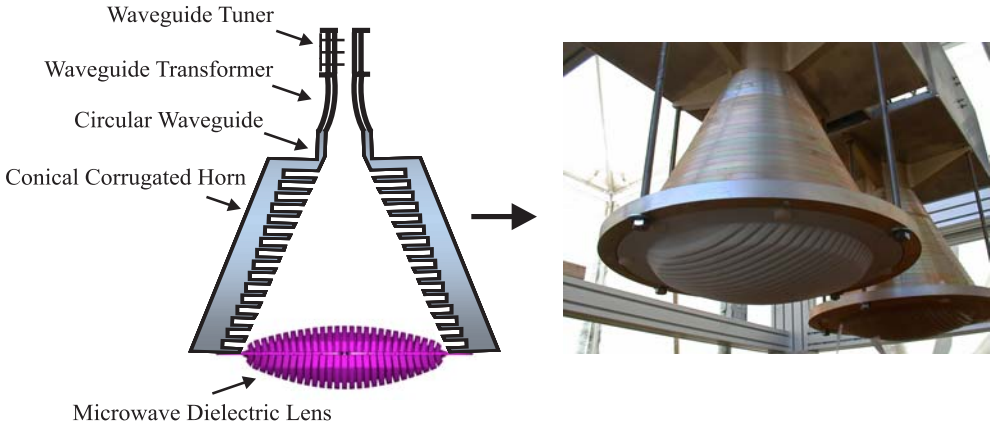

Figure 2. A diagram and a photograph of the lens-focused corrugated horn.

the surface of the earth and the mine to be displaced. The motion of the mine is quite different than the surrounding soil because the mechanical properties of the mine are quite different than those of the soil. The displacement of the surface of the earth when the mine is present is different than when it is not present because of waves scattered from the mine. The array of radars detects these displacements and thus the mine.

The theoretical model and design of the antenna are presented in section 2. Theoretical and measured patterns for the antennas are presented in section 3. These results show that the antenna functions as designed when a matching layer is placed on the lens. In sections 4 and 5, the results for an array of two radars that was developed and tested in the experimental and field models for the elastic/seismic mine detection systems. These results show the viability of the array concept.

2. FOCUSED ANTENNA

A lens-focused conical corrugated horn has been developed for use in the mine detection system. A diagram of this antenna is shown in Fig. 2. It consists of a waveguide tuner, a waveguide transformer, conical corrugated horn and a dielectric bifocal lens. The lens and the waveguide transformer are connected by the conical metal horn with a corrugated interior. The antenna is fed from a standard rectangular waveguide, and a waveguide transformer is used to transform the rectangular waveguide to the circular waveguide. The cross section of the transformer changes gradually from a rectangular shape to a circular one. A waveguide-type tuner is used in order to match the antenna by achieving the standing wave ratio (SWR) of the antenna desired for the measurement. The waveguide-type tuner

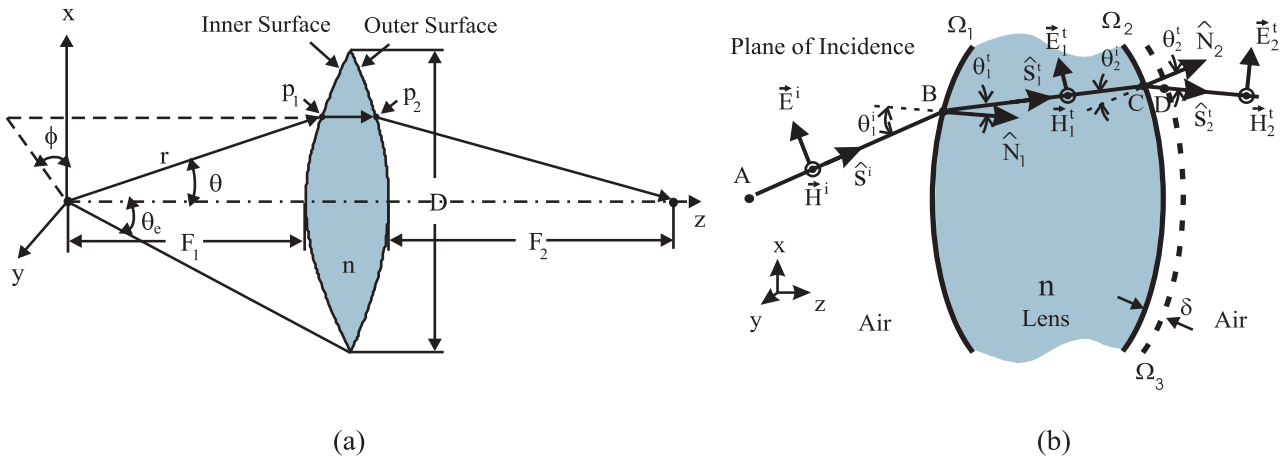

Figure 3. (a) Lens geometry and its coordinate system and (b) refraction of the ray at the lens interfaces.

consists of a standard rectangular waveguide and with three screws inserted into it. By rotating these screws, a match can be obtained. This antenna is monostatic so that this antenna functions as both a transmitter and a receiver.

A theoretical model was developed for this antenna. This model is shown in Fig. 3(a). The dielectric lens with a refraction index, n, and a diameter, D, has two focal lengths, F_1 and F_2 (inner and outer focal lengths). The diameter is confined by the semi-flare angle, θ_e of the horn. The inner focal point is the same as the phase center of the horn. The inner and outer surfaces are hyperbolic curves. The lens profile is a function of the diameter, the focal length, and the refraction index and is rotationally symmetric. Given those parameters with $\phi = 0^o (y = 0)$, the geometry of the inner surface of the lens can be defined as[10]

$$x = r \sin\theta, \qquad 0 \le \theta \le \theta_e, \tag{1}$$

$$z = \frac{a_1 n + \sqrt{(a_1 n)^2 - (n^2-1)(a_1^2 - x^2)}}{n^2 - 1}, \tag{2}$$

where $a_1 = (n-1) f_1$. The geometry of the outer surface of the lens can be given in a similar manner.

The inner surface of the lens is illuminated by a spherical wave front emanating from the horn. The horn is excited by the TE_{11} mode propagating in the circular waveguide. The TE_{11} mode is converted into the hybrid HE_{11} mode by the discontinuity between the circular waveguide and the horn and facilitated by the corrugations in the horn.[10] The electric field on the inner surface of the lens can then be described in terms of the geometric parameters by:

$$\vec{E}(\theta, \phi, r) = \left(\frac{P_\nu^1(\cos\theta)}{\sin\theta} + \frac{dP_\nu^1(\cos\theta)}{d\theta} \right) (\cos\phi\hat{\theta} - \sin\phi\hat{\phi}) \frac{e^{-jk_0 r}}{r}, \tag{3}$$

where $P_\nu^1(\cos\theta)$ is the associated Legendre function of the first kind.[11] ν is determined by the solution of the equation:

$$\frac{P_\nu^1(\cos\theta_e)}{\sin\theta_e} + \frac{dP_\nu^1(\cos\theta_e)}{d\theta_e} = 0. \tag{4}$$

The field on the outer surface of the lens is found by ray tracing. The refraction of the ray at the lens interfaces is obtained using ray tracing. Figure 3(b) illustrates the refraction of the ray ignoring reflections from the surfaces of the lens. The lens with a refraction index, n, is placed in the air. Incident fields, $\vec{E}^i$ and $\vec{H}^i$, in the direction of $\hat{s}^i$ emanate from the source at the point A, and are obtained from Eq. (3). The incident fields are partially reflected and transmitted at B. The transmitted fields, $\vec{E}_1{}^t$ and $\vec{H}_1{}^t$, propagate through within the lens in the direction of $\hat{s_1}{}^t$. Then, $\vec{H}_1{}^t$ and $\vec{E}_1{}^t$ at the location just before C can be derived from geometrical optics[12]:

$$\vec{H}_1{}^t \Big|_{\text{just before } C} = (DF_1) e^{-jk_2 \overline{BC}} \vec{H}^i \Big|_{\text{just before } B}, \tag{5}$$

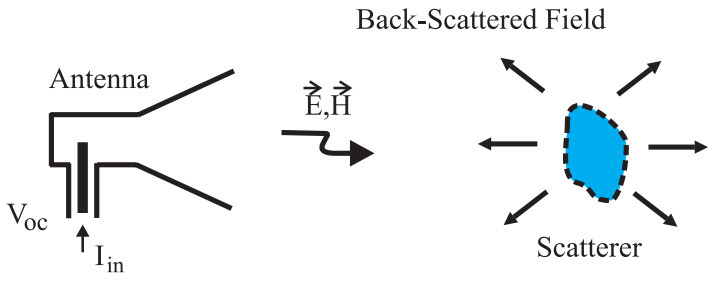

Figure 4. A receiving antenna in the presence of a scatterer.

$$\vec{E_1}^{\,t}\Big|_{\text{just before } C} = -\eta_2 \hat{s_1}^{\,t} \times \vec{H_1}^{\,t}\Big|_{\text{just before } C}, \tag{6}$$

where k_2 and η_2 are the wave number and the intrinsic impedance in the lens, respectively, DF_1 is the divergence factor of the surface Ω_1,[12] and $\overline{BC}$ is the path length between B and C.

The second refraction occurs at the interface of Ω_2. In a similar manner, the transmitted fields, $\vec{E_2}^{\,t}$ and $\vec{H_2}^{\,t}$, on the interface of Ω_3 can be obtained from

$$\vec{H_2}^{\,t}\Big|_{\text{at } D} = (DF_2)e^{-jk_1\delta}\vec{H_1}^{\,t}\Big|_{\text{just before } C}, \tag{7}$$

$$\vec{E_2}^{\,t}\Big|_{\text{at } D} = -\eta_1 \hat{s_2}^{\,t} \times \vec{H_2}^{\,t}\Big|_{\text{at } D}, \tag{8}$$

where k_1 and η_1 are the wave number and the intrinsic impedance in the free space, respectively, DF_2 is the divergence factor of the surface Ω_2, and δ is the path length between C and D. δ is infinitesimal resulting in $DF_2 \simeq 1$ and $e^{-jk_1\delta} \simeq 1$. Divergence factors were obtained using the procedure described in the literature.[13]

Once the fields on the outer surface of the lens are found by ray tracing, the outer surface of the lens can be replaced by an imaginary surface that contains the equivalent electric and magnetic surface current densities ($\vec{J_s}$ and $\vec{M_s}$) on the surface by using the equivalence theorem.[12] The imaginary surface must be presumed to be very close to the outer surface of the lens (Ω_3 in Fig. 3(b)). The equivalent electric and magnetic surface current densities can be determined from the electric and magnetic fields on the outer surface:

$$\vec{J_s} = \hat{N_2} \times \vec{H_3}, \tag{9}$$

$$\vec{M_s} = -\hat{N_2} \times \vec{E_3}. \tag{10}$$

From these, the radiation pattern of the lens can be found. The electric and magnetic fields at the position $\vec{R}$ on the observation plane may be represented by the following current-field direct relationships[14]:

$$\vec{E}(\vec{R}) = \frac{-j\omega\mu_0}{4\pi}\iint_{s'}[\vec{J_s}\Psi + \frac{1}{k_0^2}(\vec{J_s}\cdot\nabla')\nabla'\Psi]ds' - \frac{1}{4\pi}\iint_{s'}(\vec{M_s}\times\nabla'\Psi)ds', \tag{11}$$

$$\vec{H}(\vec{R}) = \frac{-j\omega\epsilon_0}{4\pi}\iint_{s'}[\vec{M_s}\Psi + \frac{1}{k_0^2}(\vec{M_s}\cdot\nabla')\nabla'\Psi]ds' + \frac{1}{4\pi}\iint_{s'}(\vec{J_s}\times\nabla'\Psi)ds', \tag{12}$$

where $\Psi = \frac{e^{-jk_o r}}{r}$ and $\nabla' = \frac{\partial}{\partial x'}\hat{x} + \frac{\partial}{\partial y'}\hat{y} + \frac{\partial}{\partial z'}\hat{z}$. Here, x', y', and z' are defined by the coordinate system of the source. The radiated pattern (one-way pattern) of the antenna is then given by $|\vec{E}(\vec{R})|$.

Rather than the one-way pattern of the antenna, it is the two-way pattern involving the reflection from a scatterer back to the antenna that is of interest for the spot size of the antenna when the antenna is used with the radar to measure surface displacements. This is because radar is monostatic, and the antenna is used for both transmitting and receiving. The two-way pattern can be easily obtained by introducing a scatterer in the presence of the antenna.[15]

Table 1. Predetermined parameters for the lens and the horn.

Diameter of the horn aperture, D	20 cm
Phase center of the horn from the aperture	23.46 cm
Semi-flare angle of the horn, θ_e	23.09 degrees
Diameter of the lens, D	20 cm
Dielectric constant of the lens, ϵ_r	2.53
Operating frequency, f	8 GHz
Polarization of the excited wave	Linear
Height of the antenna, h	20 cm

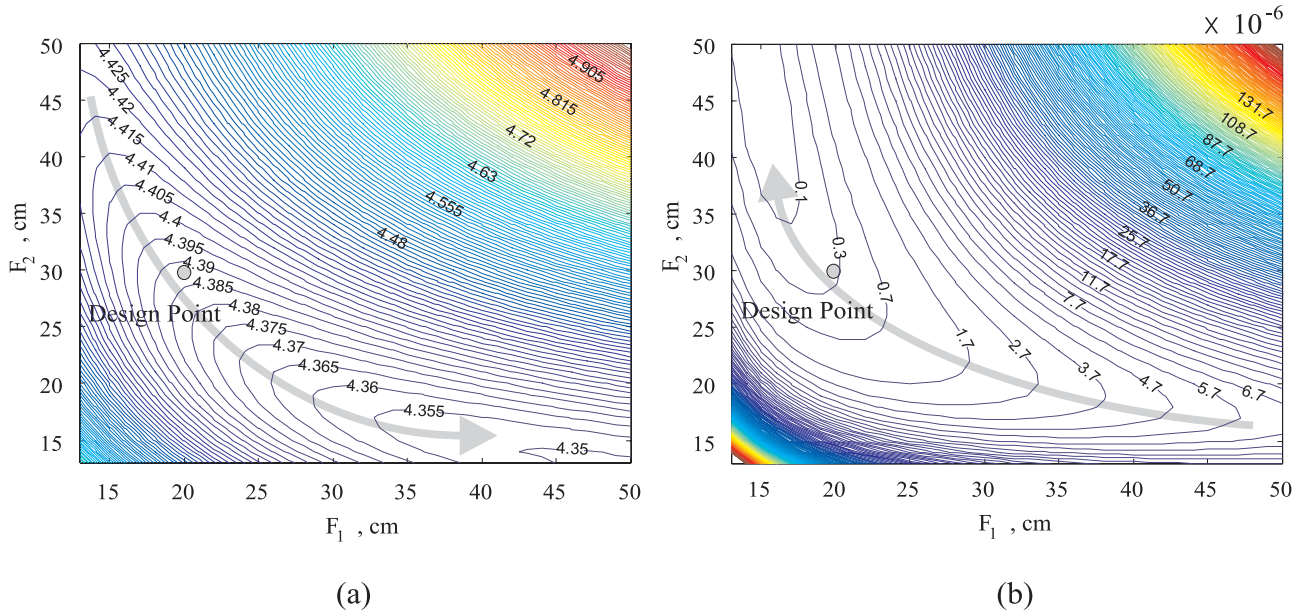

Figure 5. Contour graphs of the 3 dB spot size in centimeters (a) and the normalized sidelobe levels (b) of the lens-focused corrugated horn antenna with $D = 20$ cm.

Figure 4 is a diagram showing a receiving antenna with a scatterer. Here, I_{in} is an input current to the antenna, and $\vec{E}(\vec{R})$ and $\vec{H}(\vec{R})$ are the fields at the position $\vec{R}$ radiated by the antenna without the scatterer. When the scatterer exists, the antenna receives the fields scattered back from the scatterer. Let the scatterer be a sphere with radius $a \ll \lambda_0$, and the sphere is assumed to be located at the position $\vec{R}$. Then, using the reciprocity theorem, the received open-circuit voltage of the antenna in the presence of the scatterer can be expressed as[15]

$$V_{oc} = -j\omega\epsilon_0 4\pi a^3 \frac{\epsilon - \epsilon_0}{\epsilon + 2\epsilon_0} \frac{|\vec{E}(\vec{R})|^2}{I_{in}} + j\omega\mu_0 4\pi a^3 \frac{\mu - \mu_0}{\mu + 2\mu_0} \frac{|\vec{H}(\vec{R})|^2}{I_{in}}, \tag{13}$$

which is equivalent to the radar backscattering from the sphere. If the sphere is assumed as a perfect conductor, $\epsilon = \infty$ and $\mu = \mu_o$, resulting in

$$V_{oc} = -j\omega\epsilon_0 4\pi a^3 \frac{|\vec{E}(\vec{R})|^2}{I_{in}}. \tag{14}$$

Let the sphere be infinitesimal and be scanned over an arbitrary plane placed h apart from the lens. Then, the two-way pattern of the antenna is obtained from Eq. (14). The shape of the pattern is defined by only non-constant term, $\vec{E}(\vec{R})$. Thus, the two-way pattern can be approximated as $\alpha|\vec{E}(\vec{R})|^2$, where α is a constant that depends on the size of the scatterer and the details of how the antenna is fed.

Using the theoretical model described above, a parametric study was conducted to design a bifocal lens providing

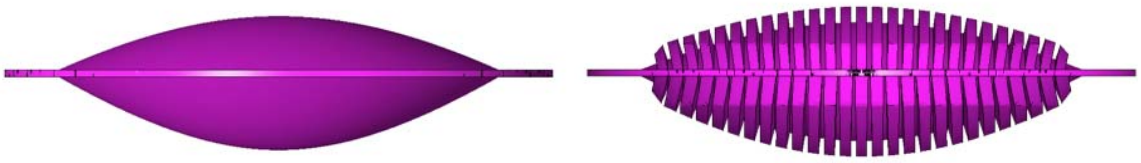

(a) (b)

Figure 6. Diagrams of dielectric lenses: (a) surface unmatched lens and (b) surface matched lens.

appropriate electrical characteristics such as focused spot size and sidelobe levels. A corrugated horn with specific dimensions was selected. Some important predetermined parameters for the horn and the lens are shown in Table. 1. With those parameters, the E-plane two-way patterns of the antenna were calculated as a function of the inner focal length, F_1, and the outer focal length, F_2, of the lens. From these two-way patterns, the 3 dB spot size and the sidelobe level were obtained for different values of F_1 and F_2. Here, the 3 dB spot size was obtained by measuring the width of the main beam in these patterns 3 dB down from the maximum, and the sidelobe level was obtained by normalizing the total energy confined in the sidelobe level by the total energy confined in the main beam. The boundary between the main beam and the sidelobe level was taken at the position of ± 10 cm from the center of the main beam. For the antenna, the contour graphs of the 3 dB spot size and the sidelobe level as a function of F_1 and F_2 are shown in Fig. 5. The spot size was obtained at a standoff distance of 20 cm. The spot size indicated on each contour is shown in centimeters, and the sidelobe level is dimensionless. It is seen that the spot size decreases in the direction of the arrow, with the smallest spot size appearing on the upper left. However, along the gray line (arrow), the spot size does not change significantly. The sidelobe level behaves in the opposite manner to the spot size. The sidelobe level is seen decreasing in the direction of the arrow. It is seen that there is a tradeoff between the spot size and the sidelobe level. Consequently, an appropriate combination of two foci of the lens must be selected. These graphs were used as a tool to design a bifocal lens to be manufactured. Two foci have been selected at the design point indicated in Fig. 5.

Two types of the lens were designed and manufactured: a surface matched lens and a surface unmatched lens. These types of lenses are shown in Fig. 6. Focal lengths of 20 cm and 30 cm and the diameter of 20 cm were selected for both lenses. A surface unmatched lens was made of Rexolite 1422 material. This material has a dielectric constant of 2.53 and a loss tangent of approximately 0.001 at 8 GHz. This material maintains a dielectric constant of 2.53 through 500 GHz with a low dissipation factor. For this reason, this material is commonly used for microwave lenses and antennas. The surfaces of unmatched lenses are relatively easy to fabricate because the geometries of the surfaces of the lenses are simple hyperbolic curves and are rotationally symmetric. Thus, a CNC lathe was used to fabricate the lens.

For the surface matched lens, a quarter wavelength matching layer is usually used to match the surface of the lens, and several techniques of simulating a quarter wave matching have been reported: corrugated surfaces, arrays of dielectric cylinders, and arrays of holes in the surface of the lens.[16] For this research, corrugated surfaces with horizontal corrugations were chosen. These corrugations are perpendicular to the polarization of the excited E-field. Details of the theory and the design of the corrugations can be found in the literature.[16,17] Because of the complexities of the corrugation geometries, this lens would be costly and time consuming to manufacture using typical machining practices. For this reason, rapid prototyping machines such as a fused deposition modeling (FDM) machine and a SLA machine were used to fabricate the prototype.

Two surface matched lenses were designed and fabricated. One of these lenses was made of the polycarbonate material using the FDM machine. The electrical properties of this material, such as a dielectric constant and a loss tangent, were measured by placing a sample of the material in a waveguide and measuring the transmission coefficient through the sample. It was found that that the dielectric constant and the loss tangent are approximately 2.58 and 0.004 at 8 GHz, respectively. The polycarbonate material was chosen because this material has a very low loss factor; its loss factor is comparable to that of Rexolite 1422. A second surface matched lens was made of SL 7510 material using a SLA machine. The electrical properties of this material were measured. It was found that the

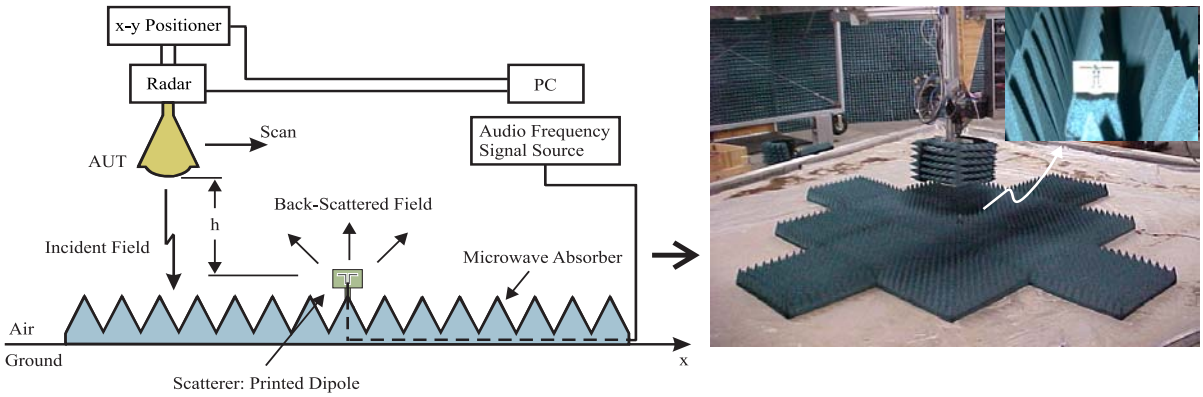

Figure 7. A schematic diagram and a photograph of the measurement setup for measuring two-way patterns of the antenna.

dielectric constant and the loss tangent are approximately 2.94 and 0.03 at 8 GHz, respectively. This material is significantly more lossy than the Rexolite or polycarbonate material.

3. MEASURING TWO-WAY PATTERNS OF THE FOCUSED ANTENNA

In order to measure the two-way pattern of the focused antenna, an experiment was conducted using the method of modulated scatterers.[18–20] Figure 7 shows the measurement setup to measure the two-way antenna pattern. The setup consists of an antenna under test (AUT), a radar, a modulating scatterer, and an audio frequency signal source. The scatterer is independently modulated using an audio frequency generated by a modulating source signal. The field incident on a small scatterer is then modulated and back-scattered. This back-scattered signal is then picked up by the AUT and coherently detected by the receiver. This received signal represents the two-way pattern of the AUT because the modulated and back-scattered signal depends on transmission from the transmitter to the scatterer, and then from the scatterer to the receiver.

A half wavelength dipole has been designed and built as the scatterer. This dipole is shown in Fig. 7. This scatterer was implemented to measure the two-way pattern of the AUT. The measurement was conducted by placing the small dipole in the center of a large anechoic surface. The dipole was driven by an audio frequency of 1 KHz with a peak to peak amplitude of 20 volts. The radar output was recorded at this frequency using two-second-integration time to build dynamic range above the noise floor. The AUT was then scanned linearly across the surface. The anechoic treatment assured that the measurement could not be contaminated by a signal or by multiple-reflected signals from the ground or from the scatterer.

Using the method of modulated scatterer, two-way patterns of the antenna shown in Fig. 2 with the different lenses were measured in a laboratory at the Georgia Institute of Technology. The antenna is placed 20 cm ($h = 20$ cm) above the modulated dipole scatterer.

Figure 8 shows the two-way patterns measured with four different frequencies for the surface unmatcehd lens made of Rexolite 1422. For all of frequencies, the E- and H-plane patterns are seen to be quite different from each other; the sidelobe levels of the H-plane pattern are seen to be wider and higher than those of the E-plane pattern. It was also found that the sidelobe levels are much higher and wider than predicted theoretically. Furthermore, the sidelobe levels are seen to change more than expected with changes in frequency.

These anomalies for the sidelobe levels are thought to happen because of an unwanted resonance within the lens; the lens is seen to act as a waveguide resonator that allows resonant fields to flow along the lateral direction inside the lens. The resonance is believed to happen mainly because of the impedance mismatch between the lens and the air. The impedance mismatch of the lens allows multiple reflections at lens interfaces. Multiple reflections from the interfaces degrade the antenna performance by increasing sidelobe levels.

Two-way patterns have been measured for the surface matched lens made of polycarbonate. Figure 9 shows the two-way patterns measured with four different frequencies. When compared to Fig. 8, the substantial reduction of

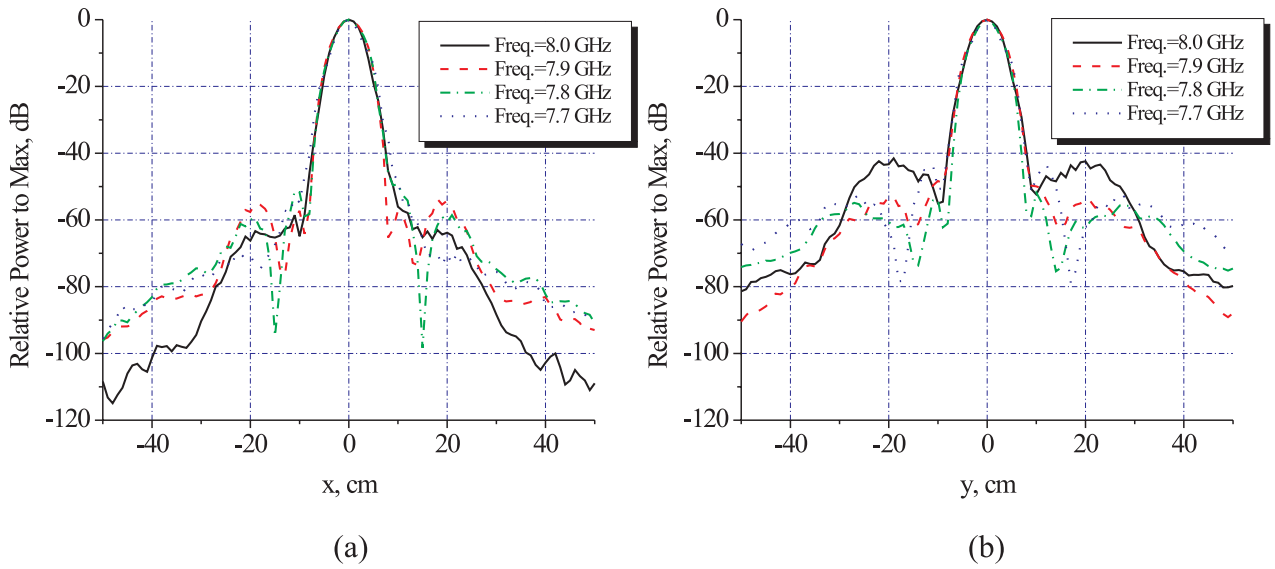

Figure 8. Measured two-way patterns of the focused antenna with the surface unmatched lens made of Rexolite 1422: (a) E-plane cut and (b) H-plane cut.

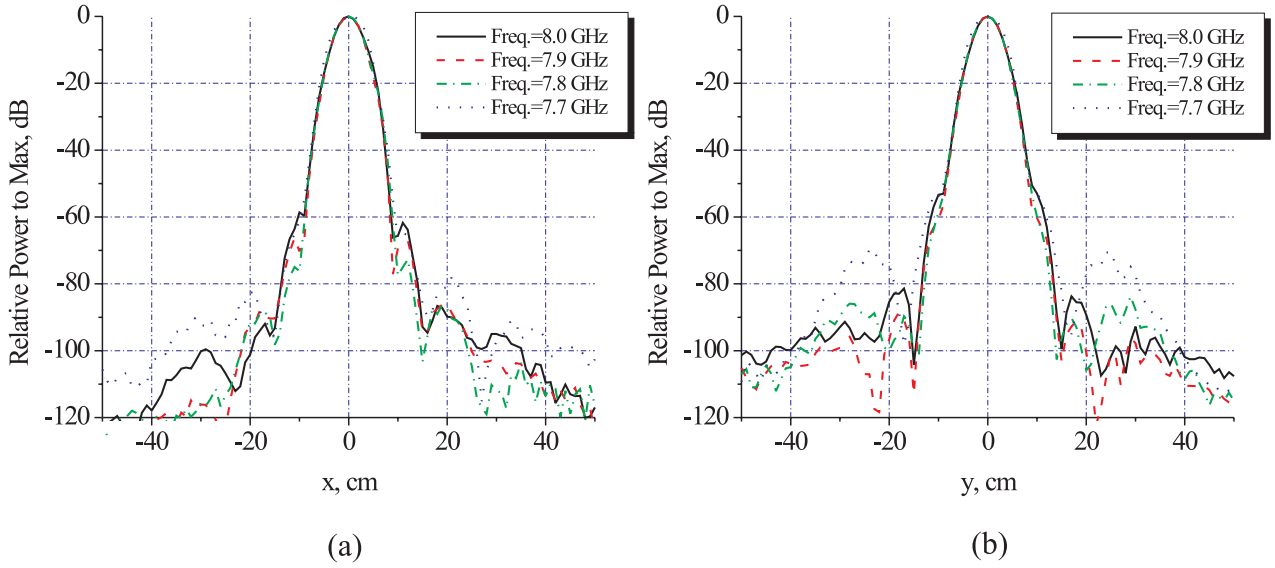

Figure 9. Measured two-way patterns of the focused antenna with the surface matched lens made of polycarbonate: (a) E-plane cut and (b) H-plane cut.

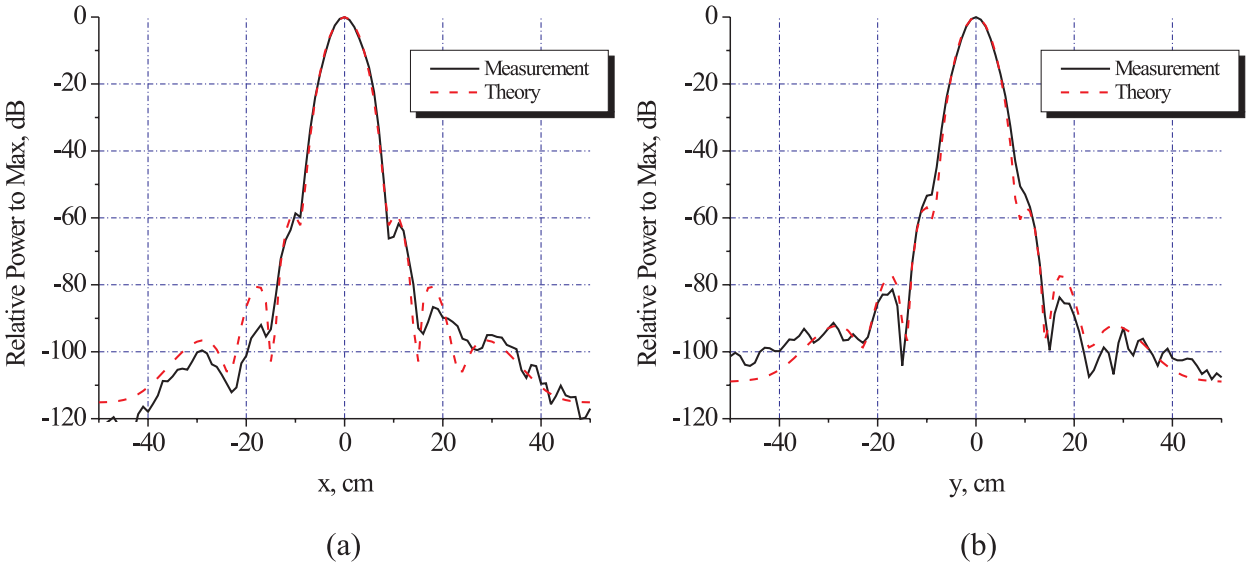

Figure 10. Comparisons between the measured and computed patterns for the surface matched lens made of polycarbonate: (a) E-plane cut and (b) H-plane cut.

the sidelobe levels is shown to be obtained with the surface matched lens. This is due to the surface matching layer, yielding the reduction of the multiple reflections within the lens.

For comparisons, the measured and calculated patterns are plotted together in Fig. 10. These comparisons are shown for the surface matched lens made of polycarbonate. The calculated patterns were obtained from the theoretical model described above ignoring the reflections from the lens surfaces and the surface matching layer. In general, the agreement is seen to be good for both planes; the first sidelobe levels and the overall shapes of the patterns are in good agreement.

The resulting patterns for the surface matched lens made of SL 7510 were seen to be slightly better than the one made of polycarbonate; the measured patterns are more consistent with the variations in the frequency, and the agreement between measured and computed patterns is better. The reason for this is that both the loss in the material and the surface matching layer contribute to the reduction of the resonance within the lens made of SL 7510. However, the maximum power received using the lens made of SL 7510 is less by approximately 3 dB than that received using the lens made of polycarbonate.

4. LABORATORY EXPERIMENTAL MODEL

In the mine detection technique being developed at Georgia Tech,[3] elastic waves are generated in the ground by an electrodynamic transducer in direct contact with the soil surface. The surface displacements are measured using a non-contacting radar sensor in a synthetic array by scanning the radar antenna over the scan region. Interactions of the elastic waves with buried landmines are used to detect the presence and location of the mines; resonant oscillations of the landmine and soil system provide a characteristic signature of the landmine, which is used as a detection cue. Previous system tests in the existing experimental model[3] have used either a waveguide antenna or a horn antenna for the radar. The use of these antennas required that either the standoff distance must be limited to a few centimeters or beamforming is needed for sufficient resolution of surface displacements. The focused antenna described in this paper was developed to allow greater standoff heights above the soil surface with similar measurement resolution without beamforming algorithms in the post-processing. To test the landmine detection capabilities of the radar using the focused antenna in an array configuration with a standoff distance of 20 cm, a two element radar array was assembled as shown in Fig. 11 and tested in the laboratory experimental model. Each antenna had a surface matched lens (one was polycarbonate, and the other was SL7510) and a separate radar source. Each source operates at a

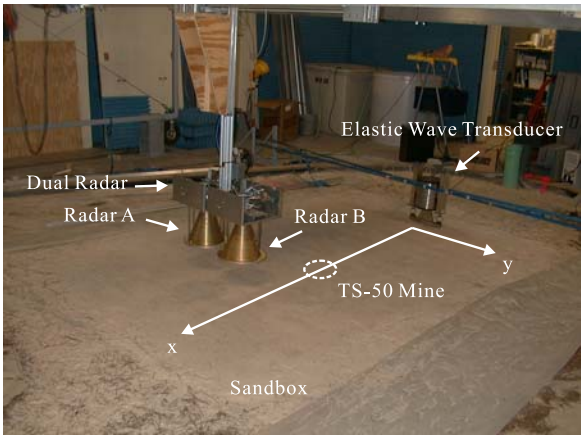

Figure 11. Measurement configuration in laboratory experimental model for detection of anti-personnel landmine.

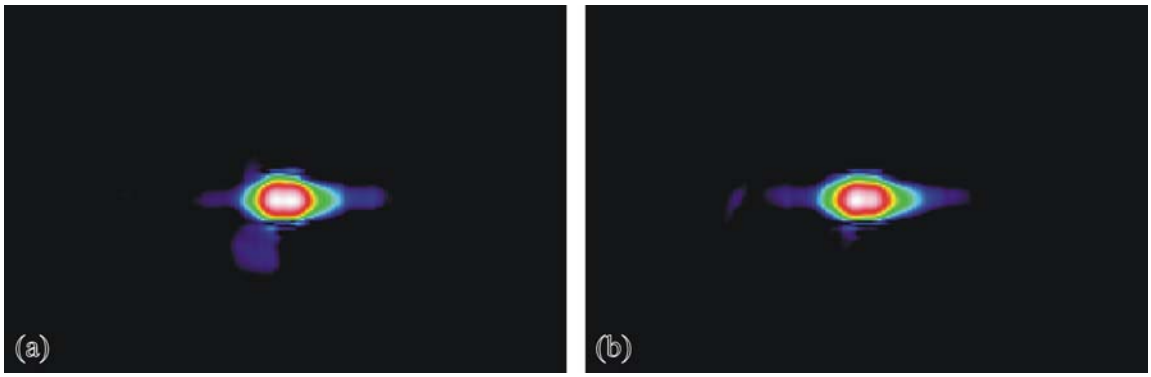

Figure 12. Detection of buried anti-personnel landmine buried 1 cm deep in the center of a 120 cm by 80 cm scan region using two different corrugated, conical radar antennas in a two element array configuration. Data are presented on a 30 dB scale: (a) using the radar with the lens made of SL 7510 and (b) using the radar with the lens made of polycarbonate.

distinct frequency of 7.8 GHz and 7.9 GHz to minimize interference between adjacent radars. Data were acquired using only one radar at a time but both sources were operating throughout the testing to include any interactions between the radars, which were found to be negligible as expected. A TS-50 anti-personnel mine was buried 1 cm deep at a distance of 1 m from the elastic wave source at a location in the center of the 120 cm by 80 cm scan region for the measurements. Each of the radars in the array produced similar results when scanned over the minefield and successfully detected the presence of the landmine; data from the two scans are plotted as images on a 30 dB scale in Fig. 12. The image processing algorithm used to form these images involves separation of the forward and reverse propagating waves to determine the reflected and scattered energy from buried objects. The energy in the reverse-propagating waves was then used as a weighting factor to improve the resolution of the image.

5. FIELD EXPERIMENTS

The dual radar array was also tested at a field test site at the Georgia Tech Research Institute's Cobb County Research Facility in Smyrna, Georgia, using the portable three-axis positioner shown in Fig. 13. The field test site was a mixture of sand, silt, and clay[21] with a significantly higher stiffness than the experimental model; this site represents the one of the stiffest soil conditions in which a landmine could reasonably be buried. Soil testing indicated that a five story building could be built at the test site without excavation. During experiments conducted with ground-contacting sensors,[22] the process of burying objects at this site was very difficult due to the existing soil conditions. To evaluate the capabilities of the radar sensor to detect landmines at the site, a TS-50 anti-personnel

Figure 13. Photographs of field testing configuration showing (a) full view of three-axis positioner and scan region and (b) dual antenna array over scan region.

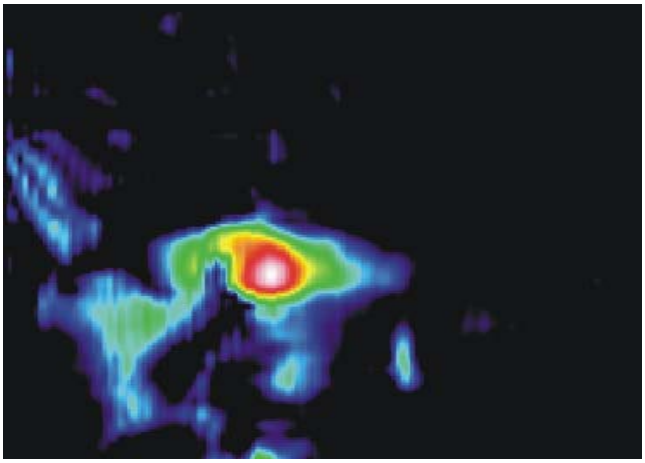

Figure 14. Detection of buried anti-personnel landmine buried 1 cm deep at a location offset from the center of a 120 cm by 80 cm scan region using a corrugated, conical radar antenna in a two element array configuration at the field test site. Data are presented on a 30 dB scale.

landmine was buried 1 cm deep 90 cm from the elastic wave source at a location slightly offset from the center of the 120 cm by 80 cm scan region. The image formed from the data measured with one of the two radars in the dual radar array indicates the location of the landmine on a 30 dB scale in Fig. 14. The clutter in the image immediately adjacent to the mine location was due to a hole dug in the scan region during the burial of the mine while the clutter in front of the landmine has been attributed to a possibly detached soil layer. The field site presented a layered, inhomogeneous medium for testing; inspection of the scan region after the measurements found that the region in question did not appear to be well attached to the subsurface layers. Thus, a more complicated elastic wave field than is typically seen in the experimental model is possible as multiple propagation modes, and associated interactions between modes, may be present in the soil at the field site. Ambient noise generated by aircraft from a nearby military airbase and by trains on nearby train tracks did not degrade the quality of the mine images.

6. CONCLUSIONS

A theoretical model is developed for a lens-focused, conical, corrugated, horn antenna and is validated by comparison to an experiment. The results show that the surface of the lens must be properly matched for the antenna to function as designed. A two element array of sensors was designed and built using this focused antenna. The array was tested

in the experimental models for the elastic/seismic mine detection system. The array was shown to function well in these experiments.

ACKNOWLEDGMENTS

This work was supported in part by the US Army Night Vision Electronic Systems Directorate, S&T Division, Countermine Technology Team, by the OSD MURI program by the US Army Research Office under contract DAAH04-96-0448, and by the Office of Naval Research under contract number N00014-01-1-0743.

REFERENCES

1. J. M. Sabatier and N. Xiang, "Acoustic-to-seismic coupling and detection of land mines," *Proc. Geoscience and Remote Sensing Symposium* **4**, pp. 1646–1648, July 2000.
2. J. M. Sabatier, H. E. Bass, L. N. Bolen, and K. Attenborough, "Acoustically induced seismic waves," *Journal of the Acoustical Society of America* **80**(2), pp. 646–649, Aug. 1986.
3. W. R. Scott, Jr., J. S. Martin, and G. D. Larson, "Experimental model for a seismic landmine detection system," *IEEE Trans. on Geoscience and Remote Sensing* **39**(6), pp. 1155–1164, June 2001.
4. W. R. Scott, Jr., C. T. Schröder, and J. S. Martin, "An acousto-electromagnetic sensor for locating land mines," in *Detection and Remediation Technologies for Mines and Minelike Targets III, Proc. SPIE*, vol. 3392, pp. 176–186, April 1998.
5. F. Codron, "Detection of surface waves in the ground using an acoustic method," *Masters Thesis in Mechanical Engineering, Gerogia Institute of Technology* , July 2000.
6. G. D. Larson, J. S. Martin, W. R. Scott, Jr., and C. Jia, "Air acoustic sensing of seismic waves," *Proceedings of the 139th Meeting of the Acoustical Society of America* , June 2000.
7. J. C. Cook and J. J. Wormser, "Semi-remote acoustic, electric, and thermal sensing of small buried nonmetallic," *IEEE Trans. on Geoscience Electronics* **GE-11**(3), pp. 135–152, July 1973.
8. *Feasibility of Acoustic Landmine Detection: Final Technical Report*, BBN Technical Report NO. 7677, May 1992.
9. W. R. Scott, Jr., S. H. Lee, G. D. Larson, J. S. Martin, and G. S. M. II, "Use of high-frequency seismic waves for the detection of buried land mines," in *Detection and Remediation Technologies for Mines and Minelike Targets VI, Proc. SPIE*, vol. 4394, pp. 543–552, April 2001.
10. Y. T. Lo and S. W. Lee, *Antenna Handbook: Antenna Theory*, Van Nostrand Reinhold, New York, 1993.
11. G. B. Arfken and H. J. Weber, *Mathematical Methods for Physicists*, Academic Press, 1995.
12. C. A. Balanis, *Advanced Engineering Electromagnetics*, John Wiley and Sons, 1989.
13. S. W. Lee, M. S. Sheshadri, V. Jamnejad, and R. Mittra, "Refraction at a curved dielectric interface: geometrical optics solution," *IEEE Trans. on Microwave Theory and Techniques* **MTT-30**(1), pp. 12–19, January 1982.
14. S. Silver, *Microwave Antenna Theory and Design*, McGraw-Hill, 1949.
15. R. E. Collin, *Antennas and radiowave propagation*, McGraw-Hill, 1985.
16. T. Morita and S. B. Cohn, "Microwave lens matching by simulated quarter-wave transformer," *IRE Trans. on Antennas and Propagation* **AP-4**, pp. 33–39, 1956.
17. L. J. Du and D. J. Scheer, "Microwave lens design for a conical horn antenna," *Microwave Journal* , pp. 49–52, September 1976.
18. A. M. Cullen and J. C. Parr, "A new perturbation method for measuring microwave fields in free space," *Proc. IEE* **102b**, pp. 836–844, 1955.
19. J. H. Richmond, "A modulated scattering technique for measurement of field distributions," *IRE Trans.* **MTT-3**(4), pp. 13–15, 1955.
20. R. F. Harrington, "Small resonant scatterers and their use for field measurements," *IRE Trans.* **MTT-10**(3), pp. 165–174, 1962.
21. T. Jordan and S. D. Thomson, *S&ME project report no. 1651-01-248*, January 2002.
22. G. D. Larson, J. S. Martin, W. R. Scott, Jr., G. S. M. II, and P. H. Rogers, "Characterization of elastic wave propagation in soil," *Proceedings of the SPIE* **4372**, April 2002.